
DRO-Augment Framework: Robustness by Synergizing Wasserstein Distributionally Robust Optimization and Data Augmentation

Jiaming Hu

Department of Mathematics & Statistics
Boston University
jh7453@bu.edu

Debarghya Mukherjee

Department of Mathematics & Statistics
Boston University
mdeb@bu.edu

Ioannis Ch. Paschalidis

Department of Electrical and Computer Engineering, Division of Systems Engineering
Department of Biomedical Engineering
Faculty of Computing & Data Sciences
Boston University
yannisp@bu.edu

Abstract

In many real-world applications, ensuring the robustness and stability of deep neural networks (DNNs) is crucial, particularly for image classification tasks that encounter various input perturbations. While data augmentation techniques have been widely adopted to enhance the resilience of a trained model against such perturbations, there remains significant room for improvement in robustness against corrupted data and adversarial attacks simultaneously. To address this challenge, we introduce DRO-Augment, a novel framework that integrates Wasserstein Distributionally Robust Optimization (W-DRO) with various data augmentation strategies to improve the robustness of the models significantly across a broad spectrum of corruptions. Our method outperforms existing augmentation methods under severe data perturbations and adversarial attack scenarios while maintaining the accuracy on the clean datasets on a range of benchmark datasets, including but not limited to CIFAR-10-C, CIFAR-100-C, MNIST, and Fashion-MNIST. On the theoretical side, we establish novel generalization error bounds for neural networks trained using a computationally efficient, variation-regularized loss function closely related to the W-DRO problem.

1 Introduction

Deep Neural Networks (DNNs) have become essential tools in fields such as computer vision, natural language processing, speech recognition, and autonomous systems. Their ability to model complex, non-linear relationships in large-scale datasets has led to significant progress in both research and real-world applications. By achieving state-of-the-art performance in tasks like image classification [25, 18], speech recognition [22, 10], natural language processing [35, 14], DNNs have established themselves as a core component of modern artificial intelligence.

Despite their (super)-human performance on clean datasets, DNNs are often found to be highly sensitive to noisy or adversarial inputs [34, 17]. Various studies have demonstrated that models trained

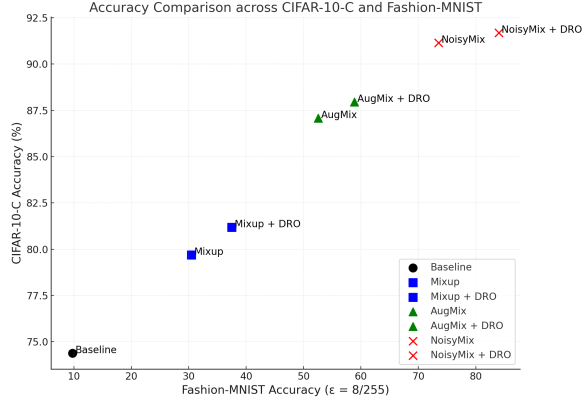


Figure 1: The PreAct ResNet-18 model trained with each standalone augmentation method with its corresponding DRO-Augment-enhanced version. DRO-augment significantly improves the test accuracy on CIFAR-10-C on Fashion-MNIST under adversarial attacks.

on unperturbed data can experience significant performance drops when tested on corrupted datasets [30], such as CIFAR-10-C and CIFAR-100-C [20] (which are corrupted versions of the CIFAR-10 and CIFAR-100 datasets, respectively), where typically the corruption is introduced by blurring, adding noise to the images, and in various other natural ways. Additionally, adversarial attacks, like Projected Gradient Descent (PGD) [28], generate small, carefully designed perturbations that can cause DNNs to make incorrect predictions with high confidence. These vulnerabilities are particularly concerning in critical applications such as autonomous driving, healthcare, and security, where model failures could have serious consequences on human life or our society as a whole.

To alleviate these issues, there is a growing interest in developing models that are more robust against various natural perturbations. One key approach for achieving this is to augment the training data with a variety of perturbations during the training of the model. Methods like Mixup [38], AugMix [21] and NoisyMix [15] aim to increase the diversity of training samples for exposing the model to a broader range of input variations. This exposure helps DNNs to generalize better to unseen perturbations and enhances their robustness against natural corruptions.

Another promising line of research aims to achieve robustness by optimizing a robust loss function. One of the most popular approaches in this area is Wasserstein distributionally robust optimization (W-DRO) [13, 29], which trains a model by minimizing the worst-case expected loss over a Wasserstein ball (the radius is denoted by ρ) centered at the empirical distribution of the training samples:

$$\min_{\beta} \sup_{\mathbb{P}: W_p(\mathbb{P}, \mathbb{Q}) \leq \rho} \mathbb{E}_{z \sim \mathbb{P}}[\ell(f_{\beta}(z))], \quad (\text{P})$$

where f is the prediction function, \mathbb{Q} is a nominal distribution, β is a parameter vector to be learned, and $\ell \in \mathcal{L}$ represents the loss function dependent on the random data z . Notable studies include robust regression models in [7, 12], adversarial training for neural networks in [33], and distributionally robust logistic regression in [32, 11]. A growing body of work has shown that W-DRO effectively penalizes a certain norm of the predictor’s gradient, leading to a formal connection between the standard W-DRO formulation (Equation (P)) and the penalized version, known as variational regularization (see [8, 12, 29, 3, 8, 9] for details). Recently, a general theory regarding the relation between this variation regularization and W-DRO has been developed in [16], which accommodates non-convex and non-smooth loss functions. W-DRO has been shown to be effective against adversarial perturbations [11, 2, 23].

Although data augmentation methods have demonstrated effectiveness against certain types of corruptions (e.g., blur, glass), our experimental results show that they remain vulnerable to others, particularly adversarial attacks. W-DRO has been shown to improve robustness against adversarial perturbations by explicitly accounting for distributional uncertainty during training. However, its impact, especially on the accuracy under natural corruptions, remains comparatively underexplored in the existing literature. Therefore, it is desirable to develop methods that are robust to both natural and adversarial corruptions.

Motivated by the complementary strengths of these two approaches, we propose DRO-Augment, a novel framework that integrates DRO with advanced data augmentation techniques to bring the best of both worlds. DRO-Augment is a training procedure that combines data augmentation methods with distributionally robust optimization by regularizing the gradient of the loss, aiming to enhance the model’s resilience to both extreme data perturbations and adversarial scenarios. Unlike standard augmentation methods, which primarily focus on improving robustness against specific types of perturbations, DRO-Augment further leverages DRO’s capacity to optimize worst-case distributions, ensuring improved robustness across a broader spectrum of distortions, without sacrificing accuracy. For a teaser, Figure 1 presents the test accuracies on CIFAR-10-C under common corruptions and on Fashion-MNIST under adversarial attacks for the PreAct ResNet-18 model, comparing each standalone augmentation method with its corresponding DRO-Augment-enhanced version. It shows that DRO-Augment provides consistent and significant robustness improvements under both natural and adversarial distribution shifts, systematically outperforming the standalone augmentation baselines. Our contributions can be summarized as follows:

1. **Novel Framework:** We propose DRO-Augment, a theoretically motivated training framework that integrates the strengths of DRO and advanced data augmentation techniques to enhance robustness against both common corruptions and adversarial attacks.
2. **Theoretical analysis:** We present a theoretical analysis of our proposed methodology demonstrating the regularization effects of DRO-Augment. In addition, we prove the asymptotic excess risk bound of combining DRO in Deep Neural Networks, providing guarantees on the generalization performance of DRO-Augment under worst-case distributional shifts.
3. **Empirical Evaluation:** Through extensive experiments on benchmark datasets (including CIFAR-10-C, CIFAR-100-C, MNIST, and Fashion-MNIST), we demonstrate that DRO-Augment significantly outperforms existing methods in terms of accuracy under severe perturbations and adversarial attacks, while maintaining performance on the clean dataset.

2 Method

Our DRO-Augment framework relies on two pillars: W-DRO and data augmentation. W-DRO aims to improve robustness against adversarial attacks by guarding against the worst-case distribution shift. Data augmentation methods, on the other hand, enhance model robustness against common corruptions by applying transformations to input images. In our framework, we first apply a chosen data augmentation method to the training data and then minimize a Wasserstein distributionally robust loss function on the augmented samples to obtain the final predictor. Our training procedure is summarized in Algorithm 1. In the following, we describe the DRO-Augment procedure in detail.

At each epoch, we begin by applying data augmentation to the training minibatch to enhance data diversity. A range of augmentation strategies has recently gained popularity for improving robustness in prediction tasks. Our framework is flexible and can accommodate any standard augmentation technique. In this work, we focus on three representative methods: Mixup [38], a widely used technique that generates new training samples by linearly interpolating between pairs of examples and their labels; AugMix [21], another widely used method that combines diverse augmentation operations (such as translation and contrast adjustment) with consistency regularization via a Jensen–Shannon divergence (JSD) loss, which is defined as the average of KL divergences between each distribution and their mean; and NoisyMix [15], a state-of-the-art approach that extends feature-level mixup with noise injection and incorporates stability training [40] to further enhance robustness.

Next, rather than minimizing the standard empirical loss over the augmented data, we optimize the training objective using a W-DRO framework. This allows the model to be optimized against worst-case perturbations within a Wasserstein ball around the empirical distribution, providing stronger guarantees under distribution shifts. Given any predictor f , the Wasserstein distributionally robust loss $D_{P_n, \rho}(f)$ is defined as:

$$D_{P_n, \rho}(f) = \sup_{\mathbb{P}: W_p(\mathbb{P}, \mathbb{P}_n) \leq \rho} \mathbb{E}_{(x, y) \sim \mathbb{P}}[\ell(f(x, y))],$$

where W_p is the L_p Wasserstein distance and \mathbb{P}_n is the empirical distribution of $\{(X_i, Y_i)\}$. While this W-DRO objective provides robustness guarantees under distribution shifts, it is generally hard to optimize directly due to the inner supremum of the Wasserstein ball constraint. To address this, we adopt a variation-regularization-based approximation of the W-DRO objective, following the

approach proposed by [16], which approximates the supremum with a gradient-norm-based penalty. This leads to the following (approximate) loss function $R_n(f)$ of $D_{P_n, \rho}(f)$:

$$R_n(f) = \mathbb{E}_{P_n}[\ell(f(x, y))] + \rho \left(\frac{1}{n} \sum_{i=1}^n \|\nabla \ell(f(x_i, y_i))\|_*^q \right)^{\frac{1}{q}}, \quad (2.1)$$

where ρ now serves as a penalty weight that controls the strength of the variation regularization. The following proposition, (Theorem 1 of [16]), provides a theoretical justification for this approximation:

Proposition 2.1 (Theorem 1 in [16]). *Let $z = (x, y) \in \mathcal{Z} = \mathcal{X} \times \mathcal{Y}$. If the gradient and Hessian norms of f are well bounded, for many important applications, it can be shown that when $\rho = O(1/\sqrt{n})$, the following asymptotic equation holds*

$$\min_f D_{P_n, \rho}(f) = \min_f \left\{ \mathbb{E}_{P_n}[\ell(f(x, y))] + \rho \left(\frac{1}{n} \sum_{i=1}^n \|\nabla \ell(f(x_i, y_i))\|_*^q \right)^{\frac{1}{q}} + O(1/n) \right\}.$$

This approximation makes it feasible to compute the W-DRO objective in practice. In our implementation, model parameters are updated using stochastic gradient descent (SGD) based on the regularization function $R_n(f)$. Over multiple epochs, the model iteratively refines its parameters to minimize both empirical risk and the regularization penalty, aiming to balance data fitting and model complexity.

Algorithm 1 Training with DRO-Augment

Require: Training data \mathcal{D} , neural network model f_θ , objective function \mathcal{L} , augmentation function \mathcal{A} , training epochs N , learning rate η , regularization weight ρ .

Initialize model parameters θ ;

for epoch = 1 to N **do**

for each minibatch $\mathcal{B} \subset \mathcal{D}$ **do**

 Apply data augmentation: $\tilde{\mathcal{B}} = \mathcal{A}(\mathcal{B})$;

for each input $(x_i, y_i) \in \tilde{\mathcal{B}}$ **do**

 Compute model output: $\hat{y}_i = f_\theta(x_i)$;

 Compute total loss:

$$\mathcal{L}_{total} = \sum_i \mathcal{L}(f_\theta(x_i), y_i) + \rho \mathbb{E}_{P_n} [\|\nabla_x \mathcal{L}(f_\theta(x_i), y_i)\|_q];$$

end for

 Update θ using stochastic gradient descent:

$$\theta \leftarrow \theta - \eta \nabla_\theta \mathcal{L}_{total};$$

end for

end for

3 Experiments

3.1 Dataset

To compare the performance of our method with other state-of-the-art methods, we conduct experiments on a suite of benchmark datasets, which are curated to evaluate the robustness of deep neural networks against common corruptions as well as adversarial attacks. The CIFAR-10-C and CIFAR-100-C datasets [20] are widely used to evaluate model robustness under synthetic/natural corruptions. These datasets are created by introducing 15 distinct types of corruption (including, but not limited to, noise, blur, weather effects, and digital distortions) to the CIFAR-10 and CIFAR-100 datasets, respectively. Each of these fifteen corruption types is applied at five predefined severity levels, which control the intensity of the corruption based on human perceptual assessment. These corrupted datasets enable a systematic analysis of model performance at various levels and types of corruption. The average classification accuracy across all corruption types and severity levels is commonly used as a metric to assess robustness (e.g., see [20, 12, 15, 38]).

To evaluate the efficacy of our method against adversarial attacks, we use the MNIST [26] and Fashion-MNIST [37] datasets, with adversarially perturbed examples generated using the Projected Gradient Descent (PGD) attack. The PGD attack [28] is a standard method for creating adversarial examples by iteratively applying small perturbations to the input within a bounded norm. The MNIST dataset consists of 70,000 grayscale images of handwritten digits (0-9) and serves as a widely used benchmark for evaluating machine learning models in the context of digit recognition. The Fashion-MNIST dataset contains 70,000 grayscale images of fashion items from 10 distinct categories, such as T-shirts, trousers, sneakers, etc. While MNIST serves as a classical baseline for simple visual pattern recognition tasks, Fashion-MNIST offers a more challenging alternative with a greater diversity of visual features. The PGD attacks target vulnerabilities in the model’s decision boundary and provide a rigorous evaluation of adversarial robustness. Unlike natural corruptions, these adversarial examples focus on the ability of models to resist malicious, worst-case perturbations crafted to deceive classifiers. The details of adversarial experiments are provided in Section 3.2

To comprehensively evaluate the robustness of our proposed framework, DRO-Augment, we use the CIFAR-10-C and CIFAR-100-C datasets to assess robustness against natural corruption, and the MNIST and Fashion-MNIST datasets to assess robustness against adversarial attacks.

3.2 Baseline and Training Details

In our experiments on the CIFAR datasets, we use three different data augmentation methods: Mixup, AugMix, and NoisyMix. For each of these augmentation methods, we also apply the corresponding DRO-Augment framework and compare their performance. We used PreActResNet-18 [19] – a variant of ResNet that applies batch normalization and ReLU activation before each convolution – for NoisyMix, Mixup, and AugMix. We train all models for 200 epochs. We also keep consistent hyperparameter configurations (e.g., learning rate, batch size, and number of epochs) across all methods for fair comparisons in the CIFAR-10-C and CIFAR-100-C experiments.

For the MNIST and Fashion-MNIST experiments, we also employed PreActResNet-18 as the primary model for all methods, with training performed over 50 epochs. Let ϵ define the maximum perturbation under the L_∞ -norm constraint. We generate adversarially corrupted images by using Projected Gradient Descent (PGD) [28] with 20 iterations, enforcing $\epsilon \in \{4/255, 8/255, 16/255\}$ and using a step size of $\epsilon/8$. We refer to the adversarially perturbed versions of MNIST and Fashion-MNIST as MNIST- ϵ and Fashion-MNIST- ϵ , respectively. As in the MNIST and Fashion-MNIST experiments, the training parameters were kept consistent across all experiments to ensure a fair and reliable comparison.

For the experimental setup, we train our models using stochastic gradient descent (SGD) with Nesterov momentum. The momentum coefficient is set to 0.9, and the weight decay is fixed at 0.0005. The initial learning rate is set to 1×10^{-1} and follows a cosine annealing schedule, gradually decaying to a minimum value of 1×10^{-5} over the course of training. We use a mini-batch size of 128 for training and a batch size of 1000 during evaluation. For data augmentation methods such as AugMix, Mixup, and NoisyMix, we adopt the recommended hyperparameter values as specified in their original papers.

All experiments are conducted on local GPU workstations equipped with two NVIDIA RTX A6000 GPUs (each with 48 GB of VRAM). For CIFAR-10-C and CIFAR-100-C, the average training time per epoch under the DRO-Augment setting is approximately 0.019 hours. For MNIST and Fashion-MNIST, each epoch completes within a few seconds due to the smaller input size and model complexity. The full implementation and all experiment scripts are publicly available at https://anonymous.4open.science/r/DRO-Augment-6F2F/Adversarial/fmnist_pgd.py.

3.3 Adversarial Attack Results

In the experiments on MNIST and Fashion-MNIST, we trained our model using the MNIST and Fashion-MNIST training sets, respectively. We introduced perturbations with different strengths ϵ set to 4/255, 8/255, and 16/255 to evaluate the effectiveness of the DRO-Augmented version in defending against varying levels of adversarial attacks. Table 1 presents a comparison of accuracy on the corrupted datasets between different data augmentation methods and their corresponding DRO-Augmented versions. On MNIST- ϵ , the DRO-Augmented version demonstrates a notable increase in robustness across different values of ϵ , without degrading standard classification accuracy,

achieving an average improvement of 7% compared to the original methods. On Fashion-MNIST- ϵ , the average robustness improvement is 5%.

Table 1: Adversarial robustness comparison under PGD attack with different ϵ values on MNIST- ϵ and Fashion-MNIST- ϵ datasets (standard deviation in parentheses).

Method	MNIST- ϵ (Acc %)			Fashion-MNIST- ϵ (Acc %)		
	$\epsilon = \frac{4}{255}$	$\epsilon = \frac{8}{255}$	$\epsilon = \frac{16}{255}$	$\epsilon = \frac{4}{255}$	$\epsilon = \frac{8}{255}$	$\epsilon = \frac{16}{255}$
Baseline	9.74	9.74	9.74	10.33	9.36	7.11
Mixup	34.85 \pm (1.64)	30.47 \pm (1.68)	22.96 \pm (2.28)	27.04 \pm (1.59)	18.37 \pm (1.46)	9.83 \pm (1.35)
Mixup + DRO	42.47 \pm (0.79)	37.49 \pm (1.14)	28.08 \pm (2.34)	33.12 \pm (1.61)	23.18 \pm (1.42)	12.09 \pm (1.18)
AugMix	55.64 \pm (2.16)	52.55 \pm (2.39)	46.03 \pm (2.62)	31.11 \pm (1.89)	24.95 \pm (1.69)	17.50 \pm (1.40)
AugMix + DRO	62.16 \pm (1.20)	58.86 \pm (1.61)	51.90 \pm (2.27)	38.87 \pm (2.29)	30.89 \pm (1.33)	20.76 \pm (1.37)
NoisyMix	73.77 \pm (1.91)	72.75 \pm (2.08)	70.88 \pm (2.09)	32.47 \pm (1.67)	28.73 \pm (1.54)	23.16 \pm (1.62)
NoisyMix + DRO	81.65 \pm (1.36)	80.87 \pm (1.43)	79.28 \pm (1.58)	37.99 \pm (0.97)	33.51 \pm (1.46)	27.00 \pm (1.15)

3.4 Common Corruption Results

As in the previous subsection, we first train the PreActResNet-18 model on the clean CIFAR-10 and CIFAR-100 datasets using various data augmentation methods, along with their corresponding DRO-Augmented versions. We then measure the accuracy of these methods on corrupted datasets (CIFAR-10-C and CIFAR-100-C).

The comparison of the results under severity level 5 for different corruption types in CIFAR-10-C and CIFAR-100-C is presented in the tables 5 and 6. Tables 7 and 8 also show a comparison of the average results across all severity levels for different corruption types in CIFAR-10-C and CIFAR-100-C. Table 9 provides a comparison of the overall average results across all severity levels and corruption types, further highlighting the performance differences between the standalone data augmentation methods and their corresponding DRO-Augmented versions. The tables 5, 6, 7, 8 and 9 are collected in Appendix D.

While the DRO-Augmented method consistently achieves higher accuracy on corrupted datasets compared to the corresponding data augmentation method across nearly all corruption types and levels (recall there are fifteen different corruption types, each with five severity levels), the improvement is particularly pronounced for the following seven corruption types: White, Shot, Impulse, Defocus, Glass, Motion, and Zoom. On these corruptions, accuracy typically improves by 2%–5%, peaking at 12.7%, with a median gain of 3.1% across all three augmentation baselines (Mixup, AugMix, NoisyMix). Notably, this robustness boost comes without sacrificing average performance. DRO-Augment still improves overall accuracy around 1.1% in the CIFAR-10-C and CIFAR-100-C datasets. Figures 2 and 3 illustrate the comparison of accuracy for the seven different corruption types mentioned above under the highest severity level (level = 5), highlighting the enhanced performance of DRO-Augmented methods over the standard augmentation methods.

3.5 Ablation study

In this subsection, we present our findings from an ablation study aimed at understanding the impact of each component, including Mixup, standard data augmentation, JSD loss, and W-DRO regularization, on the accuracy of the trained model on corrupted datasets. Towards that goal, we select CIFAR-100-C and Fashion-MNIST- ϵ as the test datasets for common corruption and adversarial attack experiments, respectively, as they offer higher complexity compared to CIFAR-10-C and MNIST. As before, we train PreAct-ResNet18 on the clean datasets (CIFAR-100 and Fashion-MNIST), assessing its robustness on the corresponding corrupted versions (CIFAR-100-C and Fashion-MNIST- ϵ with $\epsilon = 8/255$). Our results are presented in Table 2, which demonstrates that W-DRO significantly improves robustness against both common corruptions and adversarial attacks when combined with various augmentation strategies. The accuracy on CIFAR-100-C increases $\sim 1.2\%$ and on Fashion-MNIST- ϵ increases $\sim 5\%$. This highlights the advantage of combining DRO with data augmentation methods to achieve higher accuracy across a broad range of corruptions, including adversarial attacks.

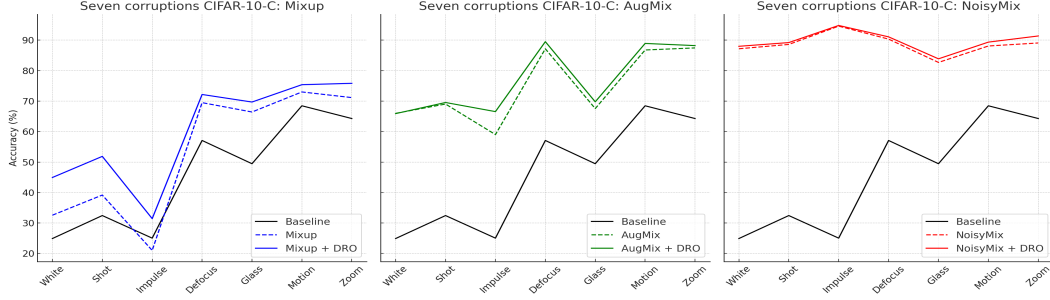


Figure 2: Performance Comparison against seven types of corruptions under Severity Level 5 on CIFAR-10-C

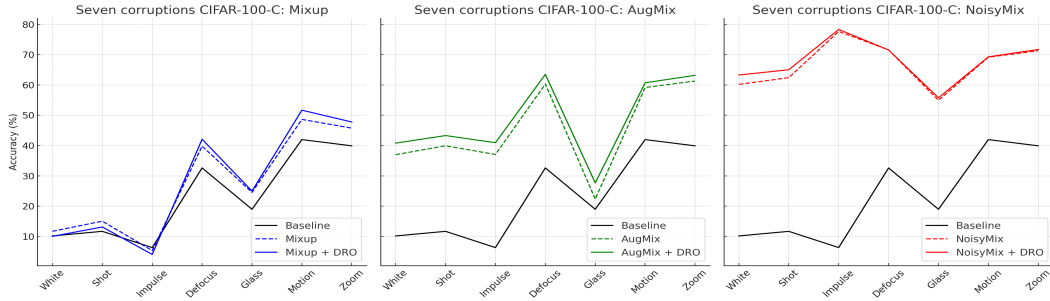


Figure 3: Performance Comparison against seven types of corruptions under Severity Level 5 on CIFAR-100-C

Table 2: Ablation study using a Preact-ResNet18 trained on CIFAR-100 and Fashion-MNIST- ϵ . The combination of W-DRO and data mixing on top of a stability training scheme on an augmented dataset boosts both robust corruption and adversarial accuracy.

Augmented Data	Mixing	JSD Loss	W-DRO	CIFAR-100-C (%)	Fashion-MNIST- $\epsilon : \epsilon = \frac{8}{255}(\%)$
×	×	×	×	47.88	9.36
×	×	×	✓	49.24	13.24
✓	×	×	×	61.28	30.46
✓	×	×	✓	62.88	35.38
×	✓	×	×	52.62	18.37
×	✓	×	✓	54.08	23.18
✓	×	✓	×	63.88	36.33
✓	×	✓	✓	65.07	44.59
✓	✓	×	×	64.29	13.86
✓	✓	×	✓	65.31	17.64
✓	✓	✓	×	67.08	17.89
✓	✓	✓	✓	67.59	21.79

4 Adversarial risk bound for neural networks

In this section, we present the asymptotic generalization error bound for a neural-network-based estimator obtained via optimizing the variation-regularized loss function $R_n(f)$ (Equation (2.1)). As illustrated in Section 2, $R_n(f)$ serves as a proxy of the W-DRO and the approximation error depends on ρ . Since our method demonstrates strong performance against L_∞ adversarial attacks, we primarily focus on the variation regularization-based approximation of the L_∞ -Wasserstein DRO

optimization problem, i.e. in our case,

$$R_n(f) = \frac{1}{n} \{ \sum_i \ell(f(x_i), y_i) + \rho \|\nabla \ell(f(x_i), y_i)\|_2 \}$$

Generalization error bounds for neural networks are crucial for understanding how well a trained model will perform on unseen data, providing theoretical guarantees that guide reliable deployment in practice. In recent years, there has been a surge of research focused on generalization error bounds for structured neural networks in nonparametric regression and classification settings (e.g., see [24, 31, 6] and references therein). To set up notations, given any $L \in \mathbb{N}$ and a vector $\mathbf{p} = (p_0, p_1, \dots, p_{L+1})$, a neural network with depth L and width vector \mathbf{p} is defined as:

$$f(x) = W_L \circ \sigma \circ W_{L-1} \circ \sigma \circ \dots \circ \sigma \circ W_0 x,$$

where $W_i \in \mathbb{R}^{p_{i+1} \times p_i}$, and each layer includes corresponding bias vectors $v_h \in \mathbb{R}^{p_{h+1}}$. The activation function σ is applied to each component of the input vector, which is taken to be $\sigma(x) = (\max\{0, x\})^2$ in our analysis. Our estimator \hat{f} is defined as:

$$\hat{f} = \arg \min_{f \in \mathcal{N}_{U, L, \mathbf{p}}^{a_1, a_2}} R_n(f). \quad (4.1)$$

where $\mathcal{N}_{U, L, \mathbf{p}}^{a_1, a_2}$ is the collection of all neural networks with depth L , width vector \mathbf{p} , with total number of active weights $U = \sum_{h=0}^L (\|W_h\|_0 + \|v_h\|_0)$, norm of gradient is almost $a_1/2$ and (operator) norm of the Hessian is almost $a_2/2$. The robust generalization error of f with respect L_∞ W-DRO loss is defined as:

$$D_{P_{\text{true}}, \rho}(f) = \sup_{Q: W_\infty(P_{\text{true}}, Q) \leq \rho} \mathbb{E}_{(x, y) \sim P_{\text{true}}} [\ell(f(x), y)] = \mathbb{E} \left[\sup_{\tilde{x}: \|x - \tilde{x}\|_2 \leq \rho} \ell(f(\tilde{x}), y) \right].$$

We denote by f_* to be the population minimizer over class of Hölder function $\mathcal{H}^\alpha(\mathbb{R}^d)$, i.e. $f_* = \arg \min_{f \in \mathcal{H}^\alpha(\mathbb{R}^d)} D_{P_{\text{true}}, \rho}(f)$, $\mathcal{H}^\alpha(\mathbb{R}^d)$ is defined as follows: To characterize the regularity of such a target function, we assume it belongs to a Hölder class $\mathcal{H}^\alpha(\mathbb{R}^d)$,

$$\mathcal{H}^\alpha(\mathbb{R}^d) = \left\{ f : \mathbb{R}^d \rightarrow \mathbb{R} \mid \max_{\|s\|_1 \leq r} \sup_{x \in \mathbb{R}^d} |\partial^s f(x)| \leq 1, \max_{\|s\|_1 = r} \sup_{x_1 \neq x_2} \frac{|\partial^s f(x_1) - \partial^s f(x_2)|}{\|x_1 - x_2\|_\infty^\alpha} \leq 1 \right\}.$$

The goal of the generalization bound is to provide an upper bound on the difference between $D_{P_{\text{true}}, \rho}(\hat{f})$ and $D_{P_{\text{true}}, \rho}(f_*)$, which we present in the following theorem:

Theorem 4.1. Assume that the population minimizer $f_* \in \mathcal{H}^\alpha(\mathbb{R}^d)$ with $\alpha > d/2$. For any fixed $Z > 0$, if we has $O(\log d + \lfloor \alpha \rfloor)$ layers, with the $\max_i p_i = O(p_{L+1} \vee d(Z + \lfloor \alpha \rfloor)^d)$ and $O(p_{L+1} d(d + \alpha)(Z + \lfloor \alpha \rfloor)^d)$ non-zero weights taking their values in $[-1, 1]$, then the optimizer \hat{f} , as defined in Equation (4.1), with ℓ -Lipschitz loss function, satisfies that there exists $c, \bar{\rho} > 0$ such that for all $\rho < \bar{\rho}$, with probability at least $1 - n^{-c}$,

$$|D_{P_{\text{true}}, \rho}(\hat{f}) - D_{P_{\text{true}}, \rho}(f_*)| \leq C_1 \left(\sqrt{\frac{\log n (U + \log U)}{n}} + U^{-\frac{\alpha}{d}} + \rho \sqrt{\frac{\log n}{n}} + \rho^2 \right).$$

If we further select $U \asymp (n / \log n)^{\frac{d}{2\alpha+d}}$, then we have

$$|D_{P_{\text{true}}, \rho}(\hat{f}) - D_{P_{\text{true}}, \rho}(f_*)| \leq C_2 \left(\left(\frac{\log n}{n} \right)^{\frac{\alpha}{2\alpha+d}} + \rho \sqrt{\frac{\log n}{n}} + \rho^2 \right),$$

where c_1, c_2, C_1, C_2 are fixed constants, depending on (α, d, a_1, a_2) .

Remark 4.2. It is worth noting that recently [27] established a similar bound on a neural network-based estimator \hat{f} . However, our analysis differs from theirs in various aspects; first, we obtain \hat{f} by minimizing the variation approximated loss $R_n(f)$, whereas [27] obtained their estimator by minimizing $D_{P_n, \rho}$ directly. Their estimator does not align with the narrative of our paper, as a central aspect of our proposed approach is to replace $D_{P, \rho}$ with its approximation R_n to facilitate optimization. Secondly, the class of neural networks considered in our theoretical analysis differs from that in [27]. Specifically, we focus on sparsely connected networks, where sparsity is imposed through conditions on U , which can be implemented via dropout in practice—in contrast to the fully connected networks studied in [27]. In addition, we employ the ReQU activation function rather than the ReLU activation used in [27]. As a result of these differences, we are able to achieve a faster rate of convergence: our estimator attains a convergence rate of $n^{-\frac{\alpha}{2\alpha+d}}$, whereas the rate established in [27] is $n^{-\frac{\alpha}{3\alpha+2d}}$.

5 Refined CIFAR-C Datasets

We aim to address the issue with the severity settings in the CIFAR-C datasets. In the original CIFAR-10-C dataset, model performance varies significantly across different corruption types, even at the same severity level. As the severity increases, this performance gap widens, with differences in accuracy exceeding 40% in extreme cases. Additionally, at severity level 1—the lowest level—most baseline models, such as ResNet-18, already achieve near-maximum accuracy, around 95%. This leaves minimal room for observing improvements, rendering severity level 1 practically uninformative.

To address this, we propose redefining the severity levels. Given that the predominant architectures used in image classification today are Transformer-based and ResNet-based models, we first designed our approach with ResNet performance in mind. We set the baseline accuracy at 50%, corresponding to the probability of random guessing in a binary decision task (e.g., 'is this class A or not?'). For the upper bound, we set the initial accuracy at approximately 85%, acknowledging that 95% represents a practical ceiling for CIFAR-10-C. This adjustment provides sufficient room to observe robustness improvements across a broader range of models.

Table 3 and 4 show that, in CIFAR-100-C, ResNet performance generally drops by approximately 30% compared to CIFAR-10-C. To account for this, we adjust our standard accuracy range downward by 30%. Specifically, we redefine the severity levels such that at severity 5, the accuracy is set at 60%, decreasing in increments of 10% down to 20% at severity 1. This proposed configuration ensures more consistent accuracy across different corruption types at the same severity level for ResNet architectures of varying depths, allowing for a more reliable evaluation of model robustness. The detailed performance of ResNet-18, ResNet-34, ResNet-50, and ResNet-101 on the refined CIFAR-10-C and CIFAR-100-C benchmarks can be found in Appendix 11.

Table 3: Performance Comparison on Refined CIFAR-10-C

Model	S1	S2	S3	S4	S5
ResNet-18	86.04	79.03	70.00	61.83	51.59
ResNet-34	86.38	79.47	70.60	62.95	52.95
ResNet-50	88.10	80.18	70.18	61.69	50.68
ResNet-101	87.60	79.54	69.51	60.85	49.74

Table 4: Performance Comparison on Refined CIFAR-100-C

Model	S1	S2	S3	S4	S5
ResNet-18	59.93	50.78	40.85	30.77	20.53
ResNet-34	57.87	49.91	41.04	31.69	21.95
ResNet-50	65.11	55.83	45.51	35.05	23.86
ResNet-101	63.80	54.58	44.65	34.53	23.87

6 Conclusion and Discussion

In our research, by combining the regularization effect of distributionally robust optimization with data augmentation methods, we enhance the model’s robustness against various corruptions and adversarial attacks in the field of computer vision classification. This approach allows the model to better handle perturbations, resulting in improved performance and reliability when faced with different types of data distribution changes. Despite its effectiveness, DRO-Augment introduces a small additional time costs due to the evaluation of the robust loss, which is not a fundamental limitation and can be mitigated through engineering or numerical improvements. To support more meaningful robustness evaluation, we also propose a refined version of the CIFAR-C benchmark that ensures corruption strength is consistent across different corruption types at each severity level. Future work will focus on exploring the potential of variation regularization in other models, such as diffusion models and large language models (LLMs). By investigating how variation regularization can be integrated into these models, we aim to further enhance their robustness and adaptability, expanding the applicability of our methods to a broader range of machine learning architectures and applications.

References

- [1] Martin Anthony and Peter L Bartlett. *Neural network learning: Theoretical foundations*. cambridge university press, 2009.
- [2] Xingjian Bai, Guangyi He, Yifan Jiang, and Jan Obloj. Wasserstein distributional robustness of neural networks, 2023.
- [3] Daniel Bartl, Samuel Drapeau, Jan Obloj, and Johannes Wiesel. Robust uncertainty sensitivity analysis. *arXiv preprint arXiv:2006.12022*, 4, 2020.
- [4] Peter Bartlett, Vitaly Maierov, and Ron Meir. Almost linear vc dimension bounds for piecewise polynomial networks. *Advances in neural information processing systems*, 11, 1998.
- [5] Denis Belomestny, Alexey Naumov, Nikita Puchkin, and Sergey Samsonov. Simultaneous approximation of a smooth function and its derivatives by deep neural networks with piecewise-polynomial activations. *Neural Networks*, 161:242–253, 2023.
- [6] Sohom Bhattacharya, Jianqing Fan, and Debarghya Mukherjee. Deep neural networks for nonparametric interaction models with diverging dimension. *The Annals of Statistics*, 52(6):2738–2766, 2024.
- [7] Jose Blanchet, Peter W Glynn, Jun Yan, and Zhengqing Zhou. Multivariate distributionally robust convex regression under absolute error loss. *Advances in Neural Information Processing Systems*, 32, 2019.
- [8] Jose Blanchet, Yang Kang, and Karthyek Murthy. Robust wasserstein profile inference and applications to machine learning. *Journal of Applied Probability*, 56(3):830–857, 2019.
- [9] Jose Blanchet, Karthyek Murthy, and Nian Si. Confidence regions in wasserstein distributionally robust estimation. *Biometrika*, 109(2):295–315, 2022.
- [10] William Chan, Navdeep Jaitly, Quoc Le, and Oriol Vinyals. Listen, attend and spell: A neural network for large vocabulary conversational speech recognition. In *2016 IEEE international conference on acoustics, speech and signal processing (ICASSP)*, pages 4960–4964. IEEE, 2016.
- [11] Ruidi Chen, Boran Hao, and Ioannis Paschalidis. Distributionally robust multiclass classification and applications in deep cnn image classifiers. *stat*, 1050:27, 2021.
- [12] Ruidi Chen and Ioannis Ch Paschalidis. A robust learning approach for regression models based on distributionally robust optimization. *Journal of Machine Learning Research*, 19(13):1–48, 2018.
- [13] Erick Delage and Yinyu Ye. Distributionally robust optimization under moment uncertainty with application to data-driven problems. *Operations research*, 58(3):595–612, 2010.
- [14] Jacob Devlin, Ming-Wei Chang, Kenton Lee, and Kristina Toutanova. Bert: Pre-training of deep bidirectional transformers for language understanding. In *Proceedings of the 2019 conference of the North American chapter of the association for computational linguistics: human language technologies, volume 1 (long and short papers)*, pages 4171–4186, 2019.
- [15] N Benjamin Erichson, Soon Hoe Lim, Winnie Xu, Francisco Utrera, Ziang Cao, and Michael W Mahoney. Noisymix: Boosting model robustness to common corruptions. *arXiv preprint arXiv:2202.01263*, 2022.
- [16] Rui Gao, Xi Chen, and Anton J Kleywegt. Wasserstein distributionally robust optimization and variation regularization. *Operations Research*, 72(3):1177–1191, 2024.
- [17] Justin Gilmer, Ryan P Adams, Ian Goodfellow, David Andersen, and George E Dahl. Motivating the rules of the game for adversarial example research. *arXiv preprint arXiv:1807.06732*, 2018.
- [18] Kaiming He, Xiangyu Zhang, Shaoqing Ren, and Jian Sun. Deep residual learning for image recognition. In *Proceedings of the IEEE conference on computer vision and pattern recognition*, pages 770–778, 2016.
- [19] Kaiming He, Xiangyu Zhang, Shaoqing Ren, and Jian Sun. Identity mappings in deep residual networks. In *Computer Vision–ECCV 2016: 14th European Conference, Amsterdam, The Netherlands, October 11–14, 2016, Proceedings, Part IV 14*, pages 630–645. Springer, 2016.
- [20] Dan Hendrycks and Thomas Dietterich. Benchmarking neural network robustness to common corruptions and perturbations. *arXiv preprint arXiv:1903.12261*, 2019.
- [21] Dan Hendrycks, Norman Mu, Ekin D Cubuk, Barret Zoph, Justin Gilmer, and Balaji Lakshminarayanan. Augmix: A simple data processing method to improve robustness and uncertainty. *arXiv preprint arXiv:1912.02781*, 2019.

- [22] Geoffrey Hinton, Li Deng, Dong Yu, George E Dahl, Abdel-rahman Mohamed, Navdeep Jaitly, Andrew Senior, Vincent Vanhoucke, Patrick Nguyen, Tara N Sainath, et al. Deep neural networks for acoustic modeling in speech recognition: The shared views of four research groups. *IEEE Signal processing magazine*, 29(6):82–97, 2012.
- [23] Nam Ho-Nguyen and Stephen J Wright. Adversarial classification via distributional robustness with wasserstein ambiguity. *Mathematical Programming*, 198(2):1411–1447, 2023.
- [24] Michael Kohler and Sophie Langer. On the rate of convergence of fully connected deep neural network regression estimates. *The Annals of Statistics*, 49(4):2231–2249, 2021.
- [25] Alex Krizhevsky, Ilya Sutskever, and Geoffrey E Hinton. Imagenet classification with deep convolutional neural networks. *Advances in neural information processing systems*, 25, 2012.
- [26] Yann LeCun, Léon Bottou, Yoshua Bengio, and Patrick Haffner. Gradient-based learning applied to document recognition. *Proceedings of the IEEE*, 86(11):2278–2324, 1998.
- [27] Changyu Liu, Yuling Jiao, Junhui Wang, and Jian Huang. Nonasymptotic bounds for adversarial excess risk under misspecified models. *SIAM Journal on Mathematics of Data Science*, 6(4):847–868, 2024.
- [28] Aleksander Mądry, Aleksandar Makelov, Ludwig Schmidt, Dimitris Tsipras, and Adrian Vladu. Towards deep learning models resistant to adversarial attacks. *stat*, 1050(9), 2017.
- [29] Peyman Mohajerin Esfahani and Daniel Kuhn. Data-driven distributionally robust optimization using the wasserstein metric: Performance guarantees and tractable reformulations. *Mathematical Programming*, 171(1):115–166, 2018.
- [30] Evgenia Rusak, Lukas Schott, Roland S Zimmermann, Julian Bitterwolf, Oliver Bringmann, Matthias Bethge, and Wieland Brendel. A simple way to make neural networks robust against diverse image corruptions. In *Computer Vision–ECCV 2020: 16th European Conference, Glasgow, UK, August 23–28, 2020, Proceedings, Part III 16*, pages 53–69. Springer, 2020.
- [31] Johannes Schmidt-Hieber. Nonparametric regression using deep neural networks with relu activation function. 2020.
- [32] Soroosh Shafieezadeh Abadeh, Peyman M Mohajerin Esfahani, and Daniel Kuhn. Distributionally robust logistic regression. *Advances in neural information processing systems*, 28, 2015.
- [33] Aman Sinha, Hongseok Namkoong, and John C Duchi. Certifiable distributional robustness with principled adversarial training. corr, abs/1710.10571. *arXiv preprint arXiv:1710.10571*, 2017.
- [34] Christian Szegedy, Wojciech Zaremba, Ilya Sutskever, Joan Bruna, Dumitru Erhan, Ian Goodfellow, and Rob Fergus. Intriguing properties of neural networks. *arXiv preprint arXiv:1312.6199*, 2013.
- [35] Ashish Vaswani, Noam Shazeer, Niki Parmar, Jakob Uszkoreit, Llion Jones, Aidan N Gomez, Łukasz Kaiser, and Illia Polosukhin. Attention is all you need. *Advances in neural information processing systems*, 30, 2017.
- [36] Roman Vershynin. *High-dimensional probability: An introduction with applications in data science*, volume 47. Cambridge university press, 2018.
- [37] Han Xiao, Kashif Rasul, and Roland Vollgraf. Fashion-mnist: a novel image dataset for benchmarking machine learning algorithms. *arXiv preprint arXiv:1708.07747*, 2017.
- [38] Hongyi Zhang. mixup: Beyond empirical risk minimization. *arXiv preprint arXiv:1710.09412*, 2017.
- [39] Linjun Zhang, Zhun Deng, Kenji Kawaguchi, Amirata Ghorbani, and James Zou. How does mixup help with robustness and generalization? *arXiv preprint arXiv:2010.04819*, 2020.
- [40] Stephan Zheng, Yang Song, Thomas Leung, and Ian Goodfellow. Improving the robustness of deep neural networks via stability training. In *Proceedings of the IEEE conference on computer vision and pattern recognition*, pages 4480–4488, 2016.

7 APPENDIX A: Notations

Scalars and individual data points are denoted by lowercase letters (e.g., x, y). The input-output pair is denoted by $z = (x, y)$. Prediction functions are written as $f(x)$, with associated loss $\ell(f(x), y)$ and input gradient $\nabla \ell(f(x), y)$. The true data distribution is P_{true} and the empirical distribution over n samples is P_n . Calligraphic letters (e.g., $\mathcal{H}^\alpha, \mathcal{F}$) denote function classes or sets. We use $\|\cdot\|_{q^*}$ for the dual norm of ℓ_q .

8 APPENDIX B: Auxiliary Lemmas

Lemma 8.1 ([16]). *Under the assumptions that the data distribution satisfies a bounded density condition around the set of all nondifferentiable points of $f : D_f$, there are $\bar{\rho}, J > 0$ such that for all $\rho < \bar{\rho}$, with probability at least $1 - e^{-t}$, for every f from a hypothesis family \mathcal{F} :*

$$D_{P_n, \rho}(f) = \min_{f \in \mathcal{F}} \left\{ \frac{1}{n} \sum_{i=1}^n \ell(f(x_i), y_i) + \rho \mathbb{E}_{\mathbb{P}_n} \left[\ell'(f(x), y) \|\nabla f(x)\|_* \right] \right\} \\ + \rho \sqrt{\frac{t}{2n}} + \rho^2 (J + \|H\|_{\mathbb{P}_{n,1}}) + 2\rho \mathbb{E}[\mathcal{R}_n(\mathcal{J}_\rho)]$$

where $\mathcal{J}_{\rho, \mathcal{F}} := \{x \mapsto 1\{d(x, D_f) < \rho\} : f \in \mathcal{F}, D_f \neq \emptyset\}$ and $H(x)$ is an upper bound on the operator norm of the Hessian of $f(x)$.

Lemma 8.2 ([39]). *Suppose the function class \mathcal{F} is defined over \mathcal{X} and satisfies $\sup_{f \in \mathcal{F}} \|f\|_\infty \leq D$. For any samples x_1, \dots, x_n from \mathcal{X} , we have*

$$\mathbb{E}_\sigma \left\{ \sup_{f \in \mathcal{F}} \frac{1}{n} \sum_{i=1}^n \sigma_i f(x_i) \right\} \leq \inf_{\delta \geq 0} \left\{ 4\delta + 12 \int_\delta^D \sqrt{\frac{\log \mathcal{N}(u, \mathcal{F}, L_2(P_n))}{n}} du \right\},$$

where $\sigma = (\sigma_1, \dots, \sigma_n)$ are i.i.d. Rademacher variables and $L_2(P_n)$ denotes the data-dependent L_2 metric.

Lemma 8.3 ([5], Theorem 1). *Fix $\alpha > 2$ and $p, d \in \mathbb{N}$. Then, for any function $f : [0, 1]^d \rightarrow \mathbb{R}^p$ with $f \in \mathcal{H}^\alpha([0, 1]^d)$, for any integer $Z \geq 2$, there exists a neural network h_f with ReQU activations such that it has $\mathcal{O}(\log d + \lfloor \alpha \rfloor)$ layers, at most $\mathcal{O}(p \vee d(Z + \lfloor \alpha \rfloor)^d)$ neurons per layer, and $\mathcal{O}(p(d\alpha + d^2(Z + \lfloor \alpha \rfloor)^d))$ nonzero weights in $[-1, 1]$, satisfying*

$$\|f - h_f\|_{\mathcal{H}^\ell([0, 1]^d)} \leq \frac{C^{\alpha d} \alpha^\ell}{Z^{\alpha - \ell}} \quad \text{for all } \ell \in \{0, \dots, \lfloor \alpha \rfloor\}.$$

Lemma 8.4 ([4], Theorem 2.1). *For any positive integers $U, k \leq U, L \leq U, l$, and p , considering a network with real inputs, up to U parameters, k computational units in L layers, a single output unit (identity activation), and all other units with piecewise polynomial activation of degree l and p breakpoints, the VC-dimension satisfies*

$$\text{VCdim}(\text{sgn}(\mathcal{F})) \leq 2UL \log(2eULpk) + 2UL^2 \log(l + 1) + 2L.$$

Furthermore, since $L, k = \mathcal{O}(U)$, for fixed l and p :

$$\text{VCdim}(\text{sgn}(\mathcal{F})) = \mathcal{O}(UL \log U + UL^2).$$

Lemma 8.5 ([1], Theorem 12.2). *Let \mathcal{F} be a set of real functions from a domain \mathcal{X} to $[0, M]$. Let $\varepsilon > 0$ and $\text{Pdim}(\mathcal{F})$ denote the pseudo-dimension. If $n \geq \text{Pdim}(\mathcal{F})$, then the uniform covering number satisfies*

$$\mathcal{N}_\infty(\varepsilon, \mathcal{F}, n) \leq \left(\frac{enM}{\varepsilon \text{Pdim}(\mathcal{F})} \right)^{\text{Pdim}(\mathcal{F})}.$$

Lemma 8.6 ([36], Corollary 4.2.13). *The covering numbers of the unit Euclidean ball B_2^d satisfy for any $\varepsilon \in (0, 1]$:*

$$\left(\frac{1}{\varepsilon} \right)^d \leq \mathcal{N}(B_2^d, \varepsilon) \leq \left(\frac{3}{\varepsilon} \right)^d.$$

9 APPENDIX C: Theory Proof

9.1 Risk Bound Proof

The following proof adapts the approach from [27] with modifications to account for W-DRO and the ReQu activation function.

The decomposition of the risk function is given by:

$$D_{P_{\text{true}}, \rho}(\hat{f}) - D_{P_{\text{true}}, \rho}(f^*) \\ = D_{P_{\text{true}}, \rho}(\hat{f}) - D_{P_n, \rho}(\hat{f}) + D_{P_n, \rho}(\hat{f}) - R_n(\hat{f}) + R_n(\hat{f}) - R_n(\bar{f}) + R_n(\bar{f}) - D_{P_n, \rho}(\bar{f}) \\ + D_{P_n, \rho}(\bar{f}) - D_{P_n, \rho}(f^*) + D_{P_n, \rho}(f^*) - D_{P_{\text{true}}, \rho}(f^*) \\ \leq D_{P_{\text{true}}, \rho}(\hat{f}) - D_{P_n, \rho}(\hat{f}) + D_{P_n, \rho}(\hat{f}) - R_n(\hat{f}) + R_n(\bar{f}) - D_{P_n, \rho}(\bar{f}) + D_{P_n, \rho}(\bar{f}) - D_{P_n, \rho}(f^*) \\ + D_{P_n, \rho}(f^*) - D_{P_{\text{true}}, \rho}(f^*)$$

Therefore,

$$|D_{P_{true},\rho}(\hat{f}) - D_{P_{true},\rho}(f^*)| \leq |D_{P_{true},\rho}(\hat{f}) - D_{P_n,\rho}(\hat{f})| + |D_{P_n,\rho}(\hat{f}) - R_n(\hat{f})| + |R_n(\bar{f}) - D_{P_n,\rho}(\bar{f})| \\ + |D_{P_n,\rho}(\bar{f}) - D_{P_n,\rho}(f^*)| + |D_{P_n,\rho}(f^*) - D_{P_{true},\rho}(f^*)|$$

where $\bar{f} \in \mathcal{NN}_{U,L}^{a_1,a_2}$ is the approximation of f^* , then we have

$$\begin{cases} D_{P_{true},\rho}(\hat{f}) - D_{P_n,\rho}(\hat{f}) = B_1, \\ D_{P_n,\rho}(\hat{f}) - R_n(\hat{f}) = B_2, \\ R_n(\bar{f}) - D_{P_n,\rho}(\bar{f}) = B_3, \\ D_{P_n,\rho}(\bar{f}) - D_{P_n,\rho}(f^*) = B_4, \\ D_{P_n,\rho}(f^*) - D_{P_{true},\rho}(f^*) = B_5. \end{cases}$$

9.1.1 Bound for B_2 and B_3

By Lemma 8.1, we directly derive that for any function $f \in \mathcal{NN}_{U,L}^{a_1,a_2}$ with the ReQU activation function, the following holds with probability at least $1 - e^{-t}$,

$$|R_n(f) - D_{P_n,\rho}(f)| = \rho \sqrt{\frac{t}{2n}} + \rho^2 \left(J + \frac{a_2}{2}\right)$$

Hence we can get the asymptotic bound of B_2 and B_3 .

9.1.2 Bound for B_4

Define the approximation error by

$$\mathcal{E}(\mathcal{H}^\alpha, \mathcal{NN}_{U,L}^{a_1,a_2}) = \|f - \bar{f}\|_{\mathcal{H}^0([0,1]^d)}$$

There exists $\bar{f} \in \mathcal{NN}_{U,L}^{a_1,a_2}$ approximating the target function $f^* \in \mathcal{H}^\alpha$ such that

$$\|f^* - \bar{f}\|_{\mathcal{H}^0([0,1]^d)} = O\left(\mathcal{E}(\mathcal{H}^\alpha, \mathcal{NN}_{U,L}^{a_1,a_2})\right).$$

Since ℓ is L_ℓ -Lipschitz, the difference between $D_{P_n,\rho}(f^*)$ and $D_{P_n,\rho}(\bar{f})$ satisfies

$$\begin{aligned} D_{P_n,\rho}(\bar{f}) - D_{P_n,\rho}(f^*) &\leq \frac{1}{n} \sum_{i=1}^n \left| \sup_{\|X'_i - X_i\| \leq \rho} \ell(\bar{f}(X'_i), Y_i) - \sup_{\|X'_i - X_i\| \leq \rho} \ell(f^*(X'_i), Y_i) \right| \\ &= \frac{1}{n} \sum_{i=1}^n \left| \sup_{\|X'_i - X_i\| \leq \rho} \ell(f^*(X'_i), Y_i) - \sup_{\|X'_i - X_i\| \leq \rho} \ell(\bar{f}(X'_i), Y_i) \right| \\ &\leq \frac{1}{n} \sum_{i=1}^n \sup_{\|X'_i - X_i\| \leq \rho} \left| \ell(f^*(X'_i), Y_i) - \ell(\bar{f}(X'_i), Y_i) \right| \\ &\leq L_\ell \|f^* - \bar{f}\|_{\mathcal{H}^0([0,1]^d)} \end{aligned}$$

Based on Lemma 8.3, we derive

$$B_4 \leq \frac{L_\ell C^{\alpha d}}{Z^\alpha}$$

9.1.3 Bound for B_5

For any $f \in \mathcal{H}^\alpha$ and $z = (x, y) \in \mathcal{Z}$, define

$$\tilde{\ell}(f, z) = \sup_{\|x' - x\| \leq \rho} \ell(f(x'), y).$$

We have

$$B_5 = D_{P_n,\rho}(f^*) - D_{P_{true},\rho}(f^*) \leq \sup_{f \in \mathcal{NN}_{U,L}^{a_1,a_2}} \left\{ \mathbb{E}_{P_n,\rho}[\tilde{\ell}(f, Z)] - \mathbb{E}_P[\tilde{\ell}(f, Z)] \right\}.$$

Define the class

$$\mathcal{L}^\alpha = \left\{ \tilde{\ell}(f, \cdot) : \mathcal{Z} \rightarrow \mathbb{R} \mid f \in \mathcal{H}^\alpha \right\},$$

and let the random vector $\sigma = (\sigma_1, \dots, \sigma_n)$ consist of i.i.d. Rademacher variables that are independent of the data. Denote the samples by $Z_{1:n} = \{Z_i\}_{i=1}^n$, with $Z_i = (X_i, Y_i)$. Let

$$Z'_i = (X'_i, Y'_i), \quad i = 1, \dots, n,$$

be drawn i.i.d. from P (the ghost sample). Then,

$$\begin{aligned}
& D_{P_n, \rho}(f^*) - D_{P_{true}, \rho}(f^*) \\
& \leq \sup_{f \in \mathcal{NN}_{U, L}^{a_1, a_2}} \mathbb{E}_\sigma \left\{ \mathbb{E}_{P_n, \rho}[\tilde{\ell}(f, Z)] - \mathbb{E}_P[\tilde{\ell}(f, Z)] \right\} \\
& = \sup_{f \in \mathcal{NN}_{U, L}^{a_1, a_2}} \mathbb{E}_\sigma \left\{ \frac{1}{n} \sum_{i=1}^n \tilde{\ell}(f, Z_i) - \mathbb{E}_{Z'_{1:n}} \left[\frac{1}{n} \sum_{i=1}^n \tilde{\ell}(f, Z'_i) \right] \right\} \\
& \leq \mathbb{E}_{Z'_{1:n}} \mathbb{E}_\sigma \left\{ \sup_{f \in \mathcal{NN}_{U, L}^{a_1, a_2}} \left[\frac{1}{n} \sum_{i=1}^n \tilde{\ell}(f, Z_i) - \tilde{\ell}(f, Z'_i) \right] \right\} \\
& = \mathbb{E}_\sigma \left\{ \sup_{f \in \mathcal{NN}_{U, L}^{a_1, a_2}} \frac{1}{n} \sum_{i=1}^n \sigma_i \left[\tilde{\ell}(f, Z_i) - \tilde{\ell}(f, Z'_i) \right] \right\} \\
& = \mathcal{R}_n(\mathcal{L}^\alpha).
\end{aligned}$$

Therefore, we got the $B_5 \leq \mathcal{R}_n(\mathcal{L}^\alpha)$. Because for any $f, \tilde{f} \in \mathcal{H}^\alpha$ satisfying $\|f - \tilde{f}\|_\infty \leq u/\text{Lip}^1(\ell)$, it follows

$$\begin{aligned}
\left| \tilde{\ell}(f, z) - \tilde{\ell}(\tilde{f}, z) \right| &= \left| \sup_{x' \in B_\epsilon(x)} \ell(f(x'), y) - \sup_{x' \in B_\epsilon(x)} \ell(\tilde{f}(x'), y) \right| \\
&\leq \text{Lip}^1(\ell) \sup_{x' \in B_\epsilon(x)} |f(x') - \tilde{f}(x')| \leq u.
\end{aligned}$$

Hence, we have

$$\log \mathcal{N}(u, \mathcal{L}^\alpha, \|\cdot\|_\infty) \leq \log \mathcal{N}\left(\frac{u}{\text{Lip}^1(\ell)}, \mathcal{H}^\alpha, \|\cdot\|_\infty\right).$$

Based on the Kolmogorov–Tikhomirov result (1959),

$$\log \mathcal{N}(u, \mathcal{L}^\alpha, \|\cdot\|_\infty) \lesssim u^{-d/\alpha}.$$

Let $L_2(P_n)$ denote the L_2 metric induced by the samples. Then,

$$\log \mathcal{N}(u, \mathcal{L}^\alpha, L_2(P_n)) \leq \log \mathcal{N}(u, \mathcal{L}^\alpha, \|\cdot\|_\infty) \lesssim u^{-d/\alpha}.$$

Since $\sup_{f \in \mathcal{H}^\alpha} \|f\|_\infty \leq 1$, there exists a constant B such that

$$\sup_{z \in \mathcal{Z}} |\tilde{\ell}(f, z)| \leq B \quad \text{for any } f \in \mathcal{H}^\alpha.$$

Combining this with Lemma 8.2 and the arguments in [27] (Section C.2.3), we get:

$$\begin{aligned}
\hat{\mathcal{R}}_n(\mathcal{L}^\alpha) &\lesssim \inf_{\delta \geq 0} \left\{ 4\delta + 12 \int_\delta^1 \sqrt{\frac{\log \mathcal{N}(u, \mathcal{L}^\alpha, \|\cdot\|_\infty)}{n}} du \right\} \\
&\lesssim \inf_{\delta \geq 0} \left\{ \delta + n^{-1/2} \int_\delta^1 u^{-d/(2\alpha)} du \right\} \\
&\lesssim n^{-\min\{1/2, \alpha/d\}} \log^{c(\alpha, d)} n.
\end{aligned}$$

Therefore,

$$B_5 = D_{P_n, \rho}(f^*) - D_{P_{true}, \rho}(f^*) \lesssim n^{-\min\{1/2, \alpha/d\}} \log^{c(\alpha, d)} n.$$

9.1.4 Bound for B_1

Define the class of functions \mathcal{L}_n by

$$\mathcal{L}_n = \left\{ \tilde{\ell}(f, z) : \mathcal{Z} \mapsto \mathbb{R} \mid f \in \mathcal{NN}_{U, L}^{a_1, a_2} \right\}.$$

For a given set of samples z_1, \dots, z_n from \mathcal{Z} , the empirical Rademacher complexity of class \mathcal{L}_n is defined by

$$\hat{\mathcal{R}}_n(\mathcal{L}_n) = \mathbb{E}_\sigma \left\{ \sup_{f \in \mathcal{NN}_{U, L}^{a_1, a_2}} \frac{1}{n} \sum_{i=1}^n \sigma_i \tilde{\ell}(f, z_i) \right\}.$$

As the similar logic for B_5 , we could see that

$$|D_{P_{true}, \rho}(\hat{f}) - D_{P_n, \rho}(\hat{f})| \leq \hat{\mathcal{R}}_n(\mathcal{L}_n)$$

where $\hat{f} \in \mathcal{NN}_{U,L}^{a_1,a_2}$. For any $z = (x, y) \in \mathcal{Z}$, the continuity of ℓ and f imply that there exists $\delta' \in B_\rho(0)$ such that

$$\begin{aligned}\tilde{\ell}(f, z) &= \ell(f(x + \delta'), y) - \max_j \ell(f(x + \delta_j), y) \\ &\leq \min_j |\ell(f(x + \delta'), y) - \ell(f(x + \delta_j), y)| \\ &\leq \text{Lip}^1(\ell) \text{Lip}(f) \|\delta' - \delta_j\|_\infty \\ &\leq \text{Lip}^1(\ell) \text{Lip}(f) \tau.\end{aligned}$$

Therefore, for any $f \in \mathcal{NN}_{U,L}^{a_1,a_2}$,

$$\begin{aligned}\frac{1}{n} \sum_{i=1}^n \sigma_i \tilde{\ell}(f, z_i) &= \frac{1}{n} \sum_{i=1}^n \left\{ \sigma_i \tilde{\ell}(f, z_i) - \sigma_i \max_j \ell(f(x_i + \delta_j), y_i) + \sigma_i \max_j \ell(f(x_i + \delta_j), y_i) \right\} \\ &\leq \text{Lip}^1(\ell) a_1 \tau / 2 + \frac{1}{n} \sum_{i=1}^n \left\{ \sigma_i \max_j \ell(f(x_i + \delta_j), y_i) \right\}.\end{aligned}$$

This leads to an upper bound of $\widehat{\mathcal{R}}_n(\mathcal{L}_n)$ as follows:

$$\widehat{\mathcal{R}}_n(\mathcal{L}_n) \leq \mathbb{E}_\sigma \left\{ \sup_{f \in \mathcal{NN}_{U,L}^{a_1,a_2}} \frac{1}{n} \sum_{i=1}^n \sigma_i \max_j \ell(f(x_i + \delta_j), y_i) \right\} + \text{Lip}^1(\ell) a_1 \tau / 2.$$

Define the class

$$\mathcal{L}_{n,\tau} = \left\{ \max_j \ell(f(x + \delta_j), y) : \mathcal{Z} \mapsto \mathbb{R} \mid f \in \mathcal{NN}_{U,L}^{a_1,a_2} \right\}.$$

Let $\mathcal{N}(u, \mathcal{L}_{n,\tau}, L_\infty(P_n))$ denote the covering number of the class $\mathcal{L}_{n,\tau}$ under the data-dependent L_∞ metric. Define

$$S_{n,M_\tau} = \{x_i + \delta_j : i = 1, \dots, n, j = 1, \dots, M_\tau\},$$

and let $\mathcal{N}(u, \mathcal{NN}_{U,L}^{a_1,a_2}, L_\infty(P_{nM_\tau}))$ denote the covering number of the class $\mathcal{NN}_{U,L}^{a_1,a_2}$ under the L_∞ metric on the set S_{n,M_τ} . For any $f, f' \in \mathcal{NN}_{U,L}^{a_1,a_2}$, if $\max_{i,j} |f(x_i + \delta_j) - f'(x_i + \delta_j)| \leq u$, then

$$\begin{aligned}\max_i \left| \max_j \ell(f(x_i + \delta_j), y_i) - \max_j \ell(f'(x_i + \delta_j), y_i) \right| &\leq \max_{i,j} |\ell(f(x_i + \delta_j), y_i) - \ell(f'(x_i + \delta_j), y_i)| \\ &\leq \text{Lip}^1(\ell) u.\end{aligned}$$

Hence,

$$\mathcal{N}(u, \mathcal{L}_{n,\tau}, L_\infty(P_n)) \leq \mathcal{N}(u / \text{Lip}^1(\ell), \mathcal{NN}_{U,L}^{a_1,a_2}, L_\infty(P_{nM_\tau})).$$

Suppose the functions in $\mathcal{NN}_{U,L}^{a_1,a_2}$ are uniformly bounded. Then the uniform covering number of $\mathcal{NN}_{U,L}^{a_1,a_2}$ is defined by

$$\mathcal{N}_\infty(u, \mathcal{NN}_{U,L}^{a_1,a_2}, nM_\tau) = \sup_{P_n} \mathcal{N}(u, \mathcal{NN}_{U,L}^{a_1,a_2}, L_\infty(P_{nM_\tau})),$$

where the supremum runs over all data sets of size n . Combining Lemma 8.5 and Lemma 8.4, we derive

$$\log \mathcal{N}(u, \mathcal{L}_{n,\tau}, L_\infty(P_n)) \leq \log \mathcal{N}_\infty(u, \mathcal{NN}_{U,L}^{a_1,a_2}, nM_\tau) \leq B_1 W^2 L^2 (L + \log(W^2 L)) \log(u^{-1} n M_\tau),$$

for a constant B_1 . Since $\mathcal{NN}_{U,L}^{a_1,a_2}$ is bounded and ℓ is continuous, there exists $B_2 > 0$ such that

$$\sup_{z \in \mathcal{Z}} \max_j \ell(f(x + \delta_j), y) \leq B_2 \quad \text{for any } f \in \mathcal{NN}_{U,L}^{a_1,a_2}.$$

For a given $\tau \in (0, \rho)$, let $C_{B_\rho}(\tau)$ be a $(\tau, \|\cdot\|_\infty)$ -cover of $B_\rho(0)$ with the smallest cardinality M_τ . Denote the elements of $C_{B_\rho}(\tau)$ by $\delta_1, \dots, \delta_{M_\tau}$. It follows by Lemma 8.6 that

$$\log M_\tau \leq c d \log(\rho \tau^{-1})$$

for a constant c . Combining it with Lemma 8.2, we have

$$\mathbb{E}_\sigma \left\{ \sup_{f \in \mathcal{NN}_{U,L}^{a_1,a_2}} \frac{1}{n} \sum_{i=1}^n \sigma_i \max_j \ell(f(x_i + \delta_j), y_i) \right\} \leq \inf_{\delta \geq 0} \left\{ 4\delta + 12 \int_\delta^{B_2} \sqrt{\frac{\log \mathcal{N}(u, \mathcal{L}_{n,\tau}, L_\infty(P_n))}{n}} du \right\}.$$

Hence,

$$\lesssim \inf_{\delta \geq 0} \left\{ \delta + \left(\sqrt{UL^2 + UL \log(U)} \right) n^{-1/2} \cdot \int_\delta^{B_2} \left[\sqrt{\log(u^{-1})} + \sqrt{\log n} + \sqrt{\log M_\tau} \right] du \right\}.$$

Thus,

$$\lesssim \left(\sqrt{UL^2 + UL \log(U)} \right) n^{-1/2} \left\{ \sqrt{\log n} + \sqrt{\log(\rho\tau^{-1})} \right\}.$$

Therefore, by selecting τ such that $\rho\tau^{-1} = \mathcal{O}(n)$, we show

$$|D_{P_{true},\rho}(\hat{f}) - D_{P_{n,\rho}}(\hat{f})| \lesssim \rho n^{-1} + \left(\sqrt{U + U \log(U)} \right) n^{-1/2} \sqrt{\log n}.$$

Now if we summarize them all, we get:

$$\begin{aligned} |D_{P_{true},\rho}(\hat{f}) - D_{P_{true},\rho}(f^*)| &\lesssim \frac{\alpha^d}{Z^\alpha} + \rho \sqrt{\frac{t}{2n}} + \rho^2 + n^{-\min\{1/2, \alpha/d\}} \log^{c(\alpha,d)} n + \rho n^{-1} \\ &\quad + \left(\sqrt{U + U \log(U)} \right) n^{-1/2} \sqrt{\log n}. \end{aligned}$$

10 APPENDIX D: Additional Results

Table 5: Performance comparison under severity level 5 on CIFAR-10-C (higher values are better).

Method	Noise			Blur				Weather				Digital			
	White	Shot	Impulse	Defocus	Glass	Motion	Zoom	Snow	Frost	Fog	Bright	Contrast	Elastic	Pixel	JPEG
Baseline	24.90	32.44	25.03	57.08	49.45	68.46	64.28	76.98	65.38	71.77	91.28	36.20	75.56	45.85	72.05
Mixup	32.56	39.17	21.00	69.49	66.42	73.00	71.15	83.36	82.78	81.18	90.96	65.14	80.34	61.30	76.61
Mixup + DRO	44.93	51.86	31.43	72.17	69.79	75.38	75.83	83.82	82.03	80.74	89.44	61.15	83.57	65.79	80.24
AugMix	65.98	69.03	59.01	87.16	67.54	86.77	87.45	87.53	85.04	88.92	94.06	89.29	78.97	55.52	79.22
AugMix + DRO	65.89	69.54	66.55	89.50	67.16	87.39	88.92	87.81	86.33	87.56	94.69	90.74	78.28	65.57	80.88
NoisyMix	87.17	88.59	94.60	90.34	82.69	88.08	90.79	87.81	88.74	79.16	92.58	64.03	85.83	77.42	88.63
NoisyMix + DRO	87.98	89.20	94.82	91.08	83.77	89.35	91.37	88.49	89.55	81.65	93.19	67.95	86.58	77.71	88.66

Table 6: Performance comparison under severity level 5 on CIFAR-100-C (higher values are better).

Method	Noise			Blur				Weather				Digital			
	White	Shot	Impulse	Defocus	Glass	Motion	Zoom	Snow	Frost	Fog	Bright	Contrast	Elastic	Pixel	JPEG
Baseline	10.16	11.67	6.31	32.61	18.96	41.97	39.91	44.22	33.00	37.93	65.48	17.87	47.41	23.72	40.39
Mixup	11.68	15.03	5.33	39.80	24.54	48.64	45.75	50.35	41.91	48.56	65.85	37.59	52.01	30.09	46.53
Mixup + DRO	10.02	13.11	4.05	42.09	24.97	51.68	47.78	53.78	44.07	52.15	66.30	41.20	48.71	29.08	45.51
AugMix	36.99	39.93	37.06	60.33	22.36	59.17	61.30	57.07	47.57	60.52	71.52	62.57	46.70	31.70	49.66
AugMix + DRO	40.80	43.30	40.94	63.51	27.67	60.97	63.19	58.84	51.33	58.31	72.08	65.19	47.26	30.71	50.19
NoisyMix	60.21	62.42	77.68	71.59	54.96	69.18	71.31	63.94	62.45	54.48	70.82	40.14	64.31	57.37	64.68
NoisyMix + DRO	63.30	65.03	78.34	71.57	55.77	69.30	71.73	65.27	63.62	53.62	71.13	40.98	64.09	57.98	65.51

Table 7: Performance comparison under different corruption types on CIFAR-10-C (higher values are better).

Method	Noise			Blur				Weather				Digital			
	White	Shot	Impulse	Defocus	Glass	Motion	Zoom	Snow	Frost	Fog	Bright	Contrast	Elastic	Pixel	JPEG
Baseline	44.45	57.31	56.55	83.42	54.90	79.74	79.28	82.89	78.66	88.38	93.85	77.42	84.91	74.91	79.17
Mixup	54.17	64.81	53.16	87.11	69.50	82.00	82.66	88.01	88.17	91.63	93.84	87.18	86.95	83.16	82.95
Mixup + DRO	61.67	70.88	56.42	87.36	73.35	83.21	84.80	87.59	87.46	90.33	92.64	84.88	88.03	84.55	84.71
AugMix	77.68	82.63	82.03	92.85	73.27	90.45	91.50	90.02	89.84	93.72	95.11	93.75	88.70	80.40	84.45
AugMix + DRO	78.20	83.33	85.28	93.87	73.25	91.05	92.47	91.03	91.00	93.84	95.57	94.39	89.15	85.10	85.80
NoisyMix	90.53	91.98	95.11	93.63	86.08	91.40	92.73	91.25	91.63	90.59	94.55	87.02	90.92	89.14	90.82
NoisyMix + DRO	90.95	92.42	95.33	94.12	86.87	92.20	93.27	91.55	92.16	91.61	94.93	88.28	91.47	89.33	90.88

Table 8: Performance comparison under different corruption types on CIFAR-100-C (higher values are better).

Method	Noise			Blur				Weather				Digital			
	White	Shot	Impulse	Defocus	Glass	Motion	Zoom	Snow	Frost	Fog	Bright	Contrast	Elastic	Pixel	JPEG
Baseline	21.62	29.69	24.90	60.16	20.77	53.82	53.77	54.04	48.13	63.44	73.21	54.07	60.15	51.13	49.33
Mixup	27.87	36.86	24.12	63.45	26.14	59.13	58.08	59.78	54.61	67.80	73.11	63.91	62.83	57.53	54.09
Mixup + DRO	26.17	35.94	26.26	65.97	26.56	62.01	60.58	62.87	57.26	70.51	74.97	66.31	63.53	58.11	54.14
AugMix	49.57	55.47	60.16	71.24	27.35	66.05	67.97	64.76	59.12	72.17	75.43	72.22	63.62	57.67	56.32
AugMix + DRO	52.43	57.60	61.55	72.71	33.41	67.33	69.66	66.16	61.58	71.91	75.75	73.72	63.99	57.48	56.79
NoisyMix	67.12	70.32	78.44	76.27	60.32	73.34	74.69	70.30	69.27	70.59	76.16	66.82	72.13	70.52	68.93
NoisyMix + DRO	68.93	71.78	79.01	76.63	60.94	73.50	75.03	71.26	70.01	70.41	76.40	67.14	72.01	70.92	69.49

Table 9: Average results for PreactResNet-18 models trained on CIFAR-10/100 and evaluated on CIFAR-10/100-C.

Method	CIFAR-10 ($\uparrow\%$)	CIFAR-10-C ($\uparrow\%$)	CIFAR-100 ($\uparrow\%$)	CIFAR-100-C ($\uparrow\%$)
Baseline	95.21	74.39	77.52	47.88
Mixup	95.44	79.69	79.65	52.62
Mixup + DRO	94.97	81.19	79.89	54.08
AugMix	95.55	87.09	77.42	61.28
AugMix + DRO	96.07	88.22	77.83	62.82
NoisyMix	95.37	91.15	79.62	71.01
NoisyMix + DRO	95.22	91.69	79.77	71.56

11 APPENDIX E: Refined CIFAR-C

Table 10: Accuracy of ResNet-18 on Refined CIFAR-10-C under different severity levels

Type	S1	S2	S3	S4	S5
gaussian	86.20	78.01	69.30	61.61	51.22
shot	86.51	77.16	69.00	60.36	50.88
impulse	85.01	78.65	69.19	59.73	50.82
defocus	87.03	79.53	69.27	60.50	46.63
glass	84.88	79.16	67.59	60.73	52.56
motion	85.30	78.56	70.38	60.05	52.34
zoom	85.81	79.94	71.49	64.12	54.39
snow	87.02	78.12	69.72	64.15	54.69
frost	85.86	77.90	69.68	63.13	54.17
fog	85.38	78.62	69.98	60.35	49.59
bright	86.83	80.06	71.70	62.78	52.40
contrast	86.62	81.31	71.98	63.79	52.49
elastic	85.55	78.86	69.09	59.94	51.29
pixelate	86.49	80.47	71.57	64.92	53.53
jpeg	86.18	79.03	70.01	61.33	46.79
Avg	86.04	79.03	70.00	61.83	51.59

Table 11: Accuracy of ResNet-34 on Refined CIFAR-10-C under different severity levels

Type	S1	S2	S3	S4	S5
gaussian	86.20	78.01	69.30	61.61	51.22
shot	86.51	77.16	69.00	60.36	50.88
impulse	85.01	78.65	69.19	59.73	50.82
defocus	87.03	79.53	69.27	60.50	46.63
glass	84.88	79.16	67.59	60.73	52.56
motion	85.30	78.56	70.38	60.05	52.34
zoom	85.81	79.94	71.49	64.12	54.39
snow	87.02	78.12	69.72	64.15	54.69
frost	85.86	77.90	69.68	63.13	54.17
fog	85.38	78.62	69.98	60.35	49.59
bright	86.83	80.06	71.70	62.78	52.40
contrast	86.62	81.31	71.98	63.79	52.49
elastic	85.55	78.86	69.09	59.94	51.29
pixelate	86.49	80.47	71.57	64.92	53.53
jpeg	86.18	79.03	70.01	61.33	46.79
Avg	86.04	79.03	70.00	61.83	51.59

Table 12: Accuracy of ResNet-50 on Refined CIFAR-10-C under different severity levels

Type	S1	S2	S3	S4	S5
gaussian	88.40	80.30	70.74	62.44	50.43
shot	89.17	79.85	71.92	62.72	51.95
impulse	86.97	81.18	70.95	61.20	50.78
defocus	89.28	78.65	64.31	53.83	39.72
glass	86.69	80.06	67.51	61.80	52.19
motion	87.08	78.72	69.60	59.01	49.99
zoom	87.74	79.16	68.41	59.56	48.26
snow	88.91	79.66	69.56	65.10	53.84
frost	88.10	79.13	72.06	63.32	54.37
fog	87.65	81.19	72.50	64.43	52.57
bright	88.92	81.53	71.93	62.97	52.53
contrast	88.85	83.61	75.32	67.76	57.22
elastic	86.89	79.88	70.57	60.93	51.27
pixelate	88.32	79.58	68.12	60.87	49.69
jpeg	88.53	80.15	69.14	59.44	45.43
Avg	88.10	80.18	70.18	61.69	50.68

Table 13: Accuracy of ResNet-101 on Refined CIFAR-10-C under different severity levels

Type	S1	S2	S3	S4	S5
gaussian	87.93	79.14	70.12	61.87	51.49
shot	88.16	78.44	69.57	61.25	51.38
impulse	86.71	80.30	70.53	60.33	51.44
defocus	88.89	78.76	65.34	54.08	38.82
glass	86.35	79.18	67.53	63.04	51.37
motion	86.86	78.19	69.17	57.63	48.23
zoom	87.30	79.16	68.50	60.03	48.15
snow	87.98	78.10	68.25	63.24	50.69
frost	87.43	77.59	68.63	60.51	51.59
fog	87.01	80.17	70.99	61.46	49.88
bright	88.28	80.47	69.92	60.25	50.06
contrast	88.22	82.30	73.23	65.31	54.19
elastic	86.73	79.79	69.99	60.35	51.00
pixelate	88.19	81.69	70.86	63.70	51.89
jpeg	87.94	79.82	70.00	59.66	45.87
Avg	87.60	79.54	69.51	60.85	49.74

Table 14: Accuracy of ResNet-18 on Refined CIFAR-100-C under different severity levels

Type	S1	S2	S3	S4	S5
gaussian	61.88	49.74	39.15	31.80	19.09
shot	61.45	50.45	42.01	29.19	18.49
impulse	61.29	52.34	42.23	29.00	22.49
defocus	61.01	50.95	40.08	33.01	21.55
glass	59.79	50.35	38.33	25.36	19.48
motion	59.86	52.02	41.66	32.28	20.51
zoom	57.44	48.62	40.52	29.88	18.71
snow	59.39	53.55	43.97	32.79	21.91
frost	58.51	48.81	42.59	30.20	19.89
fog	58.13	52.68	40.17	31.70	23.20
bright	58.87	52.06	41.42	29.47	20.36
contrast	60.28	51.64	39.66	32.77	21.74
elastic	59.93	49.45	40.41	32.73	19.08
pixelate	61.13	49.21	40.00	31.69	19.89
jpeg	59.99	49.76	40.59	29.75	21.60
Avg	59.93	50.78	40.85	30.77	20.53

Table 15: Accuracy of ResNet-34 on Refined CIFAR-100-C under different severity levels

Type	S1	S2	S3	S4	S5
gaussian	59.36	49.87	41.46	34.49	23.00
shot	58.79	50.88	44.08	32.15	22.51
impulse	59.12	52.33	43.06	32.07	26.45
defocus	59.26	50.70	41.72	35.83	24.92
glass	58.06	50.98	42.83	31.56	25.49
motion	58.18	51.20	41.39	32.90	21.23
zoom	56.01	48.39	41.47	31.23	19.61
snow	57.54	50.65	40.63	29.72	19.87
frost	56.44	45.89	40.51	29.81	19.59
fog	55.82	50.15	38.11	29.57	21.63
bright	57.36	49.94	39.84	28.46	20.72
contrast	58.18	48.98	37.74	31.28	20.80
elastic	57.92	48.92	40.13	31.88	18.77
pixelate	58.61	50.22	41.76	34.05	22.27
jpeg	57.45	49.58	40.81	30.37	22.37
Avg	57.87	49.91	41.04	31.69	21.95

Table 16: Accuracy of ResNet-50 on Refined CIFAR-100-C under different severity levels

Type	S1	S2	S3	S4	S5
gaussian	66.76	54.96	44.10	36.41	22.75
shot	66.23	56.02	47.55	34.17	22.47
impulse	66.29	59.35	48.46	35.49	28.00
defocus	66.02	55.38	42.41	35.78	23.08
glass	65.20	53.53	40.20	27.68	21.45
motion	64.95	55.80	44.60	34.38	20.64
zoom	62.35	52.88	43.74	32.22	19.69
snow	65.11	59.60	51.18	39.26	27.21
frost	64.19	54.81	48.72	36.35	25.50
fog	63.85	58.84	45.78	37.20	27.33
bright	64.84	58.08	48.39	36.03	25.60
contrast	65.36	58.06	47.06	40.63	28.80
elastic	64.71	53.68	44.66	36.46	21.55
pixelate	66.05	52.94	43.46	33.07	22.21
jpeg	64.71	53.56	42.33	30.69	21.55
Avg	65.11	55.83	45.51	35.05	23.86

Table 17: Accuracy of ResNet-101 on Refined CIFAR-100-C under different severity levels

Type	S1	S2	S3	S4	S5
gaussian	65.58	54.04	44.05	36.71	24.64
shot	64.83	54.97	47.32	35.17	24.26
impulse	65.32	57.01	47.40	35.29	28.20
defocus	65.11	54.15	42.78	36.00	23.80
glass	64.06	54.62	42.62	30.01	23.17
motion	64.00	54.06	43.82	34.58	21.41
zoom	61.09	51.24	42.87	31.93	20.06
snow	63.40	57.36	47.79	35.80	24.41
frost	62.37	52.55	46.55	34.92	23.44
fog	62.12	57.15	44.42	36.25	26.80
bright	62.94	56.35	46.72	34.40	25.53
contrast	63.93	56.04	44.92	39.09	27.84
elastic	63.53	53.33	43.38	35.26	21.50
pixelate	64.91	52.21	42.70	31.52	20.89
jpeg	63.81	53.60	42.42	31.03	22.07
Avg	63.80	54.58	44.65	34.53	23.87